Nano Research

ISSN 1998-0124 CN 11-5974/O4
https://doi.org/10.26599/NR.2026.94909017

Research Article

Bioinspired ion-concentration-modulated nanofluidic memristor for environment-adaptive dynamic perception

Zhuangzhuang Li, Mingzhe Zhang, Ya Lin(✉), Xuanyu Shan, Ye Tao(✉), Xiaoning Zhao, Zhongqiang Wang(✉), Haiyang Xu, Yichun Liu

State Ley Laboratory of Integrated Optoelectronics, Key Laboratory for UV Light-Emitting Materials and Technology of Ministry of Education, School of Physics, Northeast Normal University, 5268 Renmin Street, Changchun, China

Nano Res., **Just Accepted Manuscript** • https://doi.org/10.26599/NR.2026.94909017

https://www.sciopen.com/journal/1998-0124 on Jul. 10, 2026

Just Accepted

Bioinspired Ion-Concentration-Modulated Nanofluidic Memristor for Environment-Adaptive Dynamic Perception

Zhuangzhuang Li [1], Mingzhe Zhang [1], Ya Lin [1] ✉, Xuanyu Shan [1], Ye Tao [1]✉, Xiaoning Zhao [1], Zhongqiang Wang [1] ✉, Haiyang Xu [1], and Yichun Liu [1]
Northeast Normal University, China

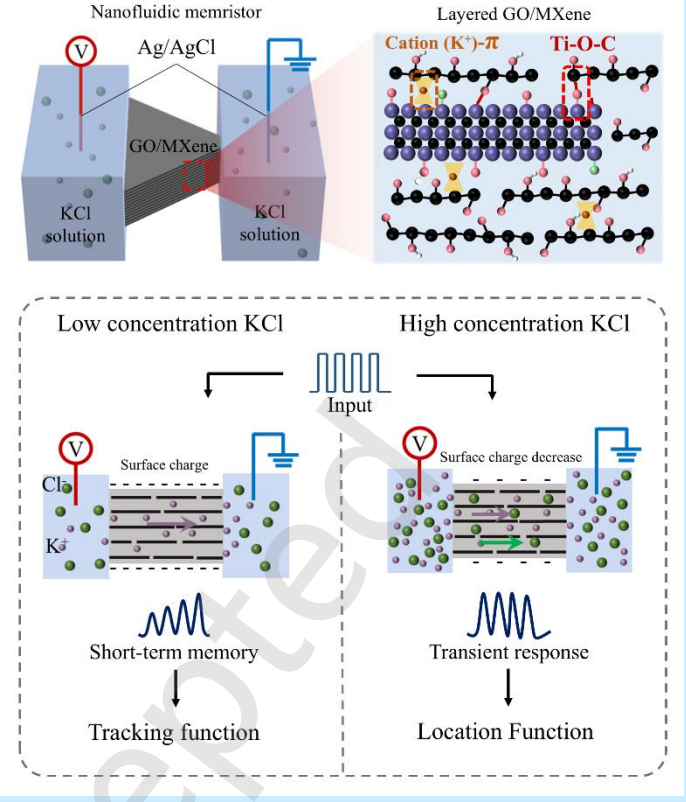

An ion-concentration-modulated nanofluidic memristor based on a graphene oxide (GO)/Mxene composite film is developed, enable emulate ion-concentration-modulated synaptic dynamics. The Ti-O-C bonds formed between GO and MXene significantly enhance the structural stability of the film in water, ensuring reliable operation for over 40 days.

[1]State Ley Laboratory of Integrated Optoelectronics, Key Laboratory for UV Light-Emitting Materials and Technology of Ministry of Education, School of Physics, Northeast Normal University, 5268 Renmin Street, Changchun, China.

Nano Research

Open Access

Review Article/Research Article Please choose on

Bioinspired ion-concentration-modulated nanofluidic memristor for environment-adaptive dynamic perception

Zhuangzhuang Li, Mingzhe Zhang, Ya Lin, Xuanyu Shan, Ye Tao, Xiaoning Zhao, Zhongqiang Wang, Haiyang Xu, and Yichun Liu

State Ley Laboratory of Integrated Optoelectronics, Key Laboratory for UV Light-Emitting Materials and Technology of Ministry of Education, School of Physics, Northeast Normal University, 5268 Renmin Street, Changchun, China

Received: 10 March 2026; **Revised:** 24 June 2026; **Accepted:** 10 July 2026

Address correspondence to Ya Lin, liny474@nenu.edu.cn; Ye Tao, taoy506@nenu.edu.cn; Zhongqiang Wang, wangzq752@nenu.edu.cn

Cite this article: *Nano Research*, 2026, 19, 94909017 https://doi.org/10.26599/NR.2026.94909017

ABSTRACT: The ion concentrations in body fluids modulate synaptic dynamics, which in turn modify perceptual capabilities and promote adaptive responses to environmental challenges. Therefore, to realize ion-concentration-modulated nanofluidic synapses is of great significance for the development of intelligent devices with environmental adaptability. We propose an ion-concentration-modulated nanofluidic memristor featuring asymmetric nanochannels based on graphene oxide (GO)/MXene composites. The Ti-O-C bonds formed between GO and MXene significantly enhance the structural stability of the thin film in water (>40 days); these results build a strong foundation for the development of nanofluidic memristors with long-term stability. At low K^+ ion concentrations (10^{-6} M), the device exhibits typical biological synaptic plasticity behaviors with strong temporal correlation, which disappear at high K^+ ion concentrations (10^{-2} M). Such an ion-concentration-modulated memristive mechanism can be attributed to the cation-π interactions between potassium ions and the material, whose concentration-dependent changes regulate surface charge and cation selectivity in the nanochannels, resulting in distinct electrical behaviors. Moreover, the dynamic neural regulation function during the predation process is demonstrated in the ion-concentration-modulated nanofluidic memristor-based neuromorphic system. This work offers a new strategy for the development of advanced functional neuromorphic devices by introducing ion concentration sensitivity for environment-adaptive dynamic perception.

KEYWORDS: ion-concentration-modulated; Nanofluidic Memristor; Asymmetric structure; dynamic perception

1. Introduction

Bioinspired neuromorphic systems, with advantages such as intelligent perception, efficient parallel processing, and low-power edge computing, represent an ideal pathway for the achievement of next-generation artificial intelligence [1-5]. To develop more intelligent neuromorphic systems, we must go beyond basic neuron/synapse imitation to include complex functions. For example, biological nerves have the abilities of multimodal perception [6-9], self-adaptability [10-13], and behavioral regulation based on chemical substance changes in the body fluid microenvironment [14-17]. Among these functions, changes in ion concentration within the body fluid microenvironment constitute an important mechanism for biological neural regulation [18-20]. Changes in ion concentrations may result from external environmental shifts [21,22], emotional states [23,24], or physiological changes [25]. These fluctuations can influence behaviors such as neuronal firing and synaptic plasticity, leading to precise perception and adaptive responses to complex dynamic environments, thus facilitating environmental adaptation [26-29]. Therefore, to develop neuromorphic devices influenced by ion concentration is fundamental to the construction of intelligent, adaptive neuromorphic systems. A hybrid ion-electronic artificial neuron was developed by integrating an electrochemical component with a solid-state memristor. This design enables wide-range tunable spiking, multimodal sensing, and biomotor nerve actuation, leveraging the high sensitivity of ionic behavior to environmental changes [30]. A bioactive ion-based switchable supercapacitor using porous carbon electrodes was developed to enable the electrically driven uptake and release of ions for concentration control and bio-interfacing applications [31]. N-shaped negative differential transconductance (NDT) was achieved in organic electrochemical transistors (OECTs) by leveraging the unique redox properties of iodide ions to enable ion-driven reconfigurability for advanced multivalued logic applications [32]. The above works highlighted the potential of ion-based technologies in the development of adaptive intelligent systems.

Nanofluidic memristors, as a novel type of ionic memristor, have emerged recently. They realize memristive behavior by manipulating ion transport within nanochannels [33,34]. This unique device structure and operating mechanism exhibit high similarity to biological nerves, making them an ideal solution for realizing neuromorphic devices [35-37]. Tang et al. developed a zinc-ion capacitor-based fluidic memristor and emulated two key forms of short-term synaptic plasticity—paired-pulse facilitation (PPF) and paired-pulse depression (PPD) — so as to realize brain-like memory functions through voltage-controlled nonlinear zinc ion plating and stripping behavior [38]. Xiao et al. developed a polarity-switchable nanofluidic memristor based on an anodized aluminum oxide (AAO) nanochannel array and achieved neural functions, including neural activation and synaptic plasticity [39]. In our previous work, we developed an optical-controlled nanofluidic artificial dendrite based on layered graphene oxide (GO) and demonstrated a neuromorphic

system mimicking the hand withdrawal reflex [40]. The above studies used nanofluidic memristors to simulate neural synapses, neurons, and dendrites, respectively. More important than simulating these fundamental neural functions is the unique liquid-phase environment and ion-migration-driven memristive mechanism of nanofluidic memristors. This enables them to replicate the ion regulatory functions observed in biological systems. For example, Xiong et al. achieved neuromorphic functions and chemical-electric signal transduction by utilizing confined polyelectrolyte-ion interactions [41]. Xu et al. realized nanofluidic synapses capable of generating bio-action potential-like spiking behaviors under the regulation of ions and neurochemical substances using a membrane based on poly (3,4-ethylenedioxythiophene) polystyrene sulfonate [42]. These studies primarily generate neuron-like spiking signals through chemical signals. Ion concentration changes are essential for environmental adaptation in biological systems, yet neuromorphic capabilities regulated by ion concentration are rarely explored.

Herein, we present an ion-concentration-modulated nanofluidic memristor that uses asymmetric GO/MXene composite films. In addition, the Ti-O-C bonds formed between GO and MXene significantly enhance the structural stability of the film and enable it to remain intact in water for over 40 days. At low K^+ ion concentrations (10^{-6} M), the device exhibits PPF, spike-duration-dependent plasticity (SDDP), and spike-rate-dependent plasticity (SRDP), demonstrating strong temporal correlation. At high concentrations (10^{-2} M), the synaptic plasticity behaviors disappear, signifying a weakening of temporal correlation. This memristive mechanism, modulated by ion concentration, stems from cation-π interactions between K^+ ions and the material. Variations in concentration alter these interactions, thereby regulating surface charge and cation selectivity within the nanochannels to produce distinct electrical behaviors. This study demonstrates that nanofluidic devices with ion concentration regulation can mimic the dynamic neural regulation function of bats during the predation process, adapting to different hunting stages. This work paves the way for the development of advanced functional neuromorphic devices by incorporating ion concentration as a critical regulatory parameter.

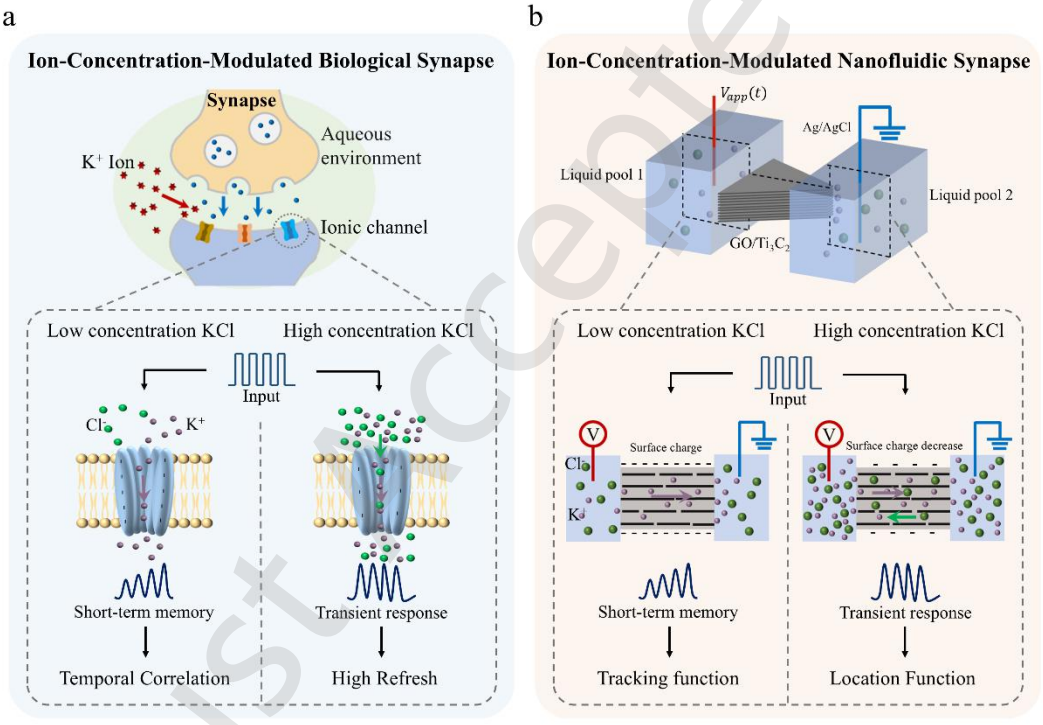

Figure 1. Ion-concentration-modulated biological synapse and nanofluidic synapse. Schematic of (a) biological synapse regulated by ion concentration dynamics and (b) nanofluidic synapse designed to mimic ion-concentration-sensitive response of biological synapses.

2. Results and discussion

Figure 1 schematically illustrates the motivation for realizing an ion-concentration-modulated nanofluidic synapse via a nanofluidic memristor. As shown in Figure 1a, in biological systems, the nervous system grows in a body fluid ionic environment, and its functions are influenced by ion concentration changes [18,43]. K^+ ions and their associated channels play a crucial role in fine-tuning neuronal excitability and synaptic behavior. Specifically, lower K^+ concentrations delay the decay of postsynaptic currents and enhance the temporal coherence of output signals, enabling short-term memory. And higher K^+ concentration augments K^+ currents, significantly increasing neuronal excitability and rendering the system highly sensitive to transient responses [44-46]. Inspired by the influence of K^+ ion concentration on synaptic plasticity in biological systems, we propose an ion-concentration-modulated nanofluidic memristor to construct a biomimetic artificial neural synapse, as shown in Figure 1b. In an environment with a low K^+ ion concentration (10^{-6} M), the nanochannels constructed from GO/MXene exhibit a highly negative surface charge, resulting in significant cation selectivity. Under continuous electrical pulse stimulation, the output current increases progressively, mimicking the short-term memory of biological synapses, indicating that the device is capable of processing temporally correlated events, such as trajectory tracking. Conversely, in the presence of a high K^+ ion concentration (10^{-2} M), the surface negativity weakens, leading to reduced cation selectivity. In this case, the output current exhibits a transient response under continuous electrical pulse stimulation, with diminished temporal correlation, making it suitable for processing transient events such as precise positioning.

Figure 2a presents a schematic illustration of our proposed

ion-concentration-modulated nanofluidic memristor (Figure S1 shows the device array, and the device-to device characteristic in the 4 × 4 nanofluidic memristive array was tested under an electrical pulse mode, as shown in Figure S17. Defining a "good bit" as a device where the current response at the 4th positive pulse is higher than that at the 1st, the array achieved a yield of 15/16. The single device was fabricated by preparing a film through vacuum filtration of a mixed GO and MXene (Ti_3C_2) dispersion (composite films with MXene mass fractions ranging from 0 to 40 wt%), followed by laser cutting into a trapezoidal shape. The film was then encapsulated with polydimethylsiloxane (PDMS), and liquid pools were created by punching holes at both ends of the film. The fabrication method for single devices is detailed in our previous work [40], while Figure S2 of the Supporting Information shows the array fabrication process. Figure 2b shows a schematic of the nanochannels formed by the interlayer gaps within the film. During the prolonged vacuum filtration process (approximately 48 hours), functional groups on the surfaces of MXene and GO react to form Ti-O-C bonds (Figure 2e). Figure 2c presents cross-sectional scanning electron microscopy (SEM) images and corresponding energy dispersive X-ray spectroscopy (EDS) mappings of C, O, K, and Cl, demonstrating a regular layered structure and cation selectivity. (Figure S3 shows the SEM and EDS mappings of other films with different ratios) Figures 2d and 2e display the XPS spectra of GO and GO/Mxene films, respectively. Notably, compared with pristine GO (Figure 2d), the composite film (10 wt%) exhibits a distinct Ti-O-C peak (at 530.4 eV) [47]. (Figure S4 presents the XPS spectra of other films). The formation of these chemical bonds effectively "locks" the layers together, thereby significantly enhancing the anti-swelling properties of the film in an aqueous environment and ensuring its long-term stability. Given the presence of these chemical bonds, we further investigated the effect of MXene content on the film properties. As shown in Figure 2f and S5, the film exhibits the minimum contact angle and optimal hydrophilicity at an MXene content of 10 wt%. However, as the MXene content increases further, the contact angle gradually increases. Additionally, the absolute value of the surface zeta potential decreases as the MXene content increases (Figure S6). This decline in hydrophilicity is attributed to the formation of additional Ti-O-C bonds, which reduces the concentration of surface oxygen-containing functional groups. Despite the reduced hydrophilicity at higher loadings, the film remains intact even after 40 days of immersion in water (Figure S7 shows the photographs and the I-V curves of devices), demonstrating remarkable enhancement of anti-swelling properties and structural stability.

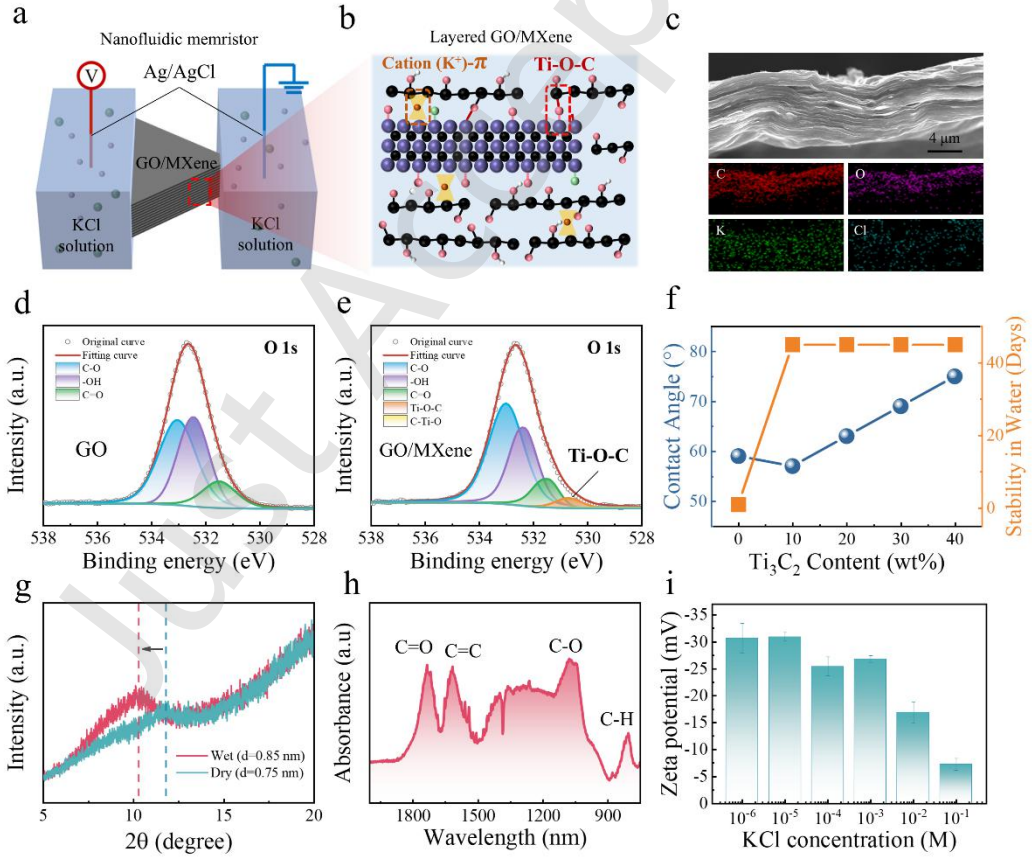

Figure 2. Structural characterization of ion-concentration-modulated nanofluidic memristor based on layered GO/MXene films. (a) Schematic of a nanofluidic memristor. (b) Schematic of layered GO/MXene films, highlighting the presence of Ti-O-C bonds and cation-π interactions. (c) Cross-sectional SEM images and EDX mapping for C, O, K, and Cl on the cross-section of layered GO/MXene films. O 1s core-level XPS spectra of (d) GO and (e) GO/MXene films, whose results indicate the formation of Ti-O-C bonds within the GO/MXene composite. (f) Contact angle and water stability (in days) of GO/MXene films with MXene content ranging from 0 to 40 wt%. (g) XRD diffraction pattern of layered GO/MXene films. (h) FT-IR absorption spectrum of GO/MXene composite. (i) Zeta potential of GO/MXene dispersion with various KCl concentrations.

Consequently, the film with 10 wt% MXene was selected for all subsequent experiments. To further verify the anti-swelling properties of the film, X-ray diffraction (XRD) was used to characterize the interlayer spacing in both dry and wet states. As shown in Figure 2g, the interlayer spacing is approximately 0.75 nm in the dry state, increasing only

marginally to 0.85 nm in the wet state. In contrast, the characteristic peak of the pristine GO film disappears completely in the wet state (Figure S8), indicating that its interlayer spacing has expanded beyond the measurement limit. This further confirms the superior anti-swelling capability of the GO/MXene film. XRD analysis reveals that while ion intercalation expands the interlayer spacing, the degree of swelling is notably suppressed at higher KCl concentrations, as shown in Figure S9. This anti-swelling behavior is attributed to the cation-π interactions, where abundant K^+ ions act as 'anchors' to lock the interlayer spaces and maintain structural stability. The Fourier transform infrared spectroscopy (FTIR) spectrum in Figure 2h reveals that the film remains rich in oxygen-containing functional groups, with characteristic peaks at 1733.8 cm^{-1} and 1076.1 cm^{-1} corresponding to respective C=O and C-O bonds, consistent with previous studies [40,47,48]. These functional groups serve both as the source of hydrophilicity and as the origin of surface negative charge. Figure 2i displays the zeta potential at various KCl concentrations, where negative values across the board confirm a negatively charged surface. As the solution concentration increases, the zeta potential rises from -35 to -5 mV, exhibiting a significant concentration dependence. This behavior is attributed to the cation-π interaction between K^+ ions, which screens the surface negative charge [49]. Such a concentration-dependent charge response lays the foundation for the device's ion concentration sensitivity.

To select the appropriate geometric dimensions, we investigated the geometric dependence of the memristive performance by varying the width of the short side (0.1 mm, 2 mm, and 6 mm). As shown in Figure S10, a distinct size-dependent behavior was observed. The device exhibits a pronounced memristive hysteresis loop only at a narrow-side width of 0.1 mm. when the width increases to 2 mm or 6 mm, the memristive character vanishes. Both experimental measurements and COMSOL simulations confirm this trend, indicating that the specific geometric confinement is a critical prerequisite for inducing the asymmetric ion transport and the resulting memristive effect in this system.

Before investigating ion concentration sensitivity, we examined the memristive characteristics and synaptic behaviors of the nanofluidic device. As illustrated in Figure 3a, under a low K^+ ion concentration (10^{-6} M), the charge carriers within the nanochannels are predominantly K^+ ions. When scanned with a sinusoidal voltage signal, the device exhibits a typical "8"-shaped hysteresis loop (Figure 3b), confirming its memristive nature. Figure S11 shows the I-V curves of other ionic concentrations, indicating that the electrical behavior of the device is influenced by the ion concentration. Furthermore, upon applying continuous positive and negative voltage scans (Figure 3c), the device current shows a continuous increase during the positive scan and a continuous decrease during the negative scan. This behavior demonstrates the device's capability to emulate synaptic short-term memory.

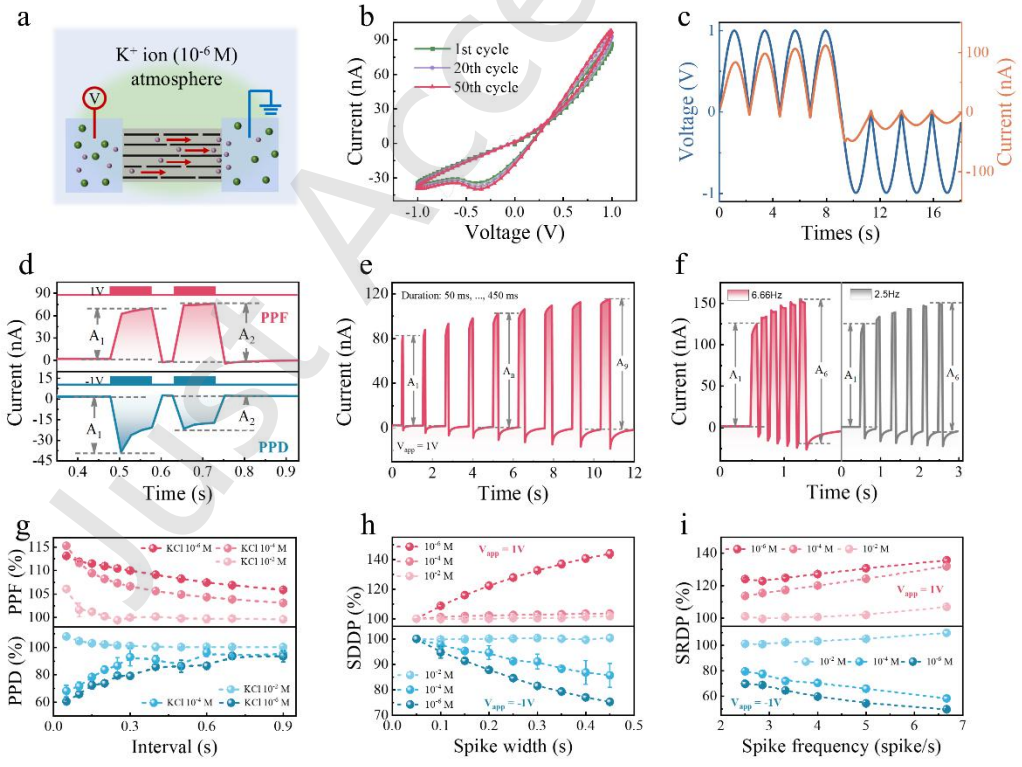

Figure 3. Demonstration of ion-concentration-modulated synaptic behaviors in nanofluidic memristor. (a) Schematic illustration of K+ ion migration within nanochannels of layered GO/MXene films under positive bias. (b) Typical I-V curves of nanofluidic memristors under low K^+ ionic concentration (10^{-6} M). (c) V-t and I-t curves of nanofluidic memristors under four consecutive positive and negative voltage pulses. (K^+ concentration: 10^{-6} M). (d) PPF and PPD functions triggered by a pair of electrical pulses with a width of 100 ms and an interval of 50 ms. (K^+ concentration: 10^{-6} M). (e) SDDP functions triggered by various pulses with widths ranging from 50 to 450 ms. (f) SRDP functions triggered by consecutive positive voltage pulses with frequencies of 6.66 and 2.5 Hz. (g-i) PPF index, PPD index ($A_2/A_1 \times 100\%$), SDDP index ($A_n/A_1 \times 100\%$), and SRDP index ($A_6/A_1 \times 100\%$) under varying K^+ concentrations (10^{-6} M, 10^{-4} M, and 10^{-2} M).

To further investigate the synaptic behavior of the nanofluidic memristor, we used electrical pulses as input signals to mimic biological presynaptic action potentials. Figure 3d presents the current response under paired-pulse stimulation,

where the red curve represents the response current under two consecutive positive electrical pulses (peak amplitude: 1 V, pulse width: 100 ms). The response current by the second pulse (A_2) is significantly higher than that of the first pulse (A_1), emulating the pair-pulse facilitation (PPF) behavior of biological synapses. The blue curve displays the response current under two consecutive negative electrical pulses (peak amplitude: -1 V, pulse width: 100 ms), where the second response current is notably lower than the first, exhibiting paired-pulse depression (PPD) behavior. Biological synaptic plasticity is influenced by both the interval between paired pulses and the pulse width (duration). As shown in Figure 3e, nine +1 V voltage pulses with durations ranging from 50 to 450 ms were applied to the device. The results demonstrate that the response current increases with the pulse duration (-1 V voltage pulses; see Figure S12 (a)), indicating significant SDDP. Pulse frequency is a key encoding mechanism for neural signals. SRDP refers to the phenomenon that synaptic connection strength changes under continuous pulse stimulation, where typically, the higher the frequency of the stimulating pulses, the more pronounced the change in synaptic weight. Figure 3f presents the SRDP realized by the nanofluidic memristor. Under 1 V pulses, the response current increases as the frequency rises from 2.5 to 6.66 Hz (represented by the A_6/A_1 ratio). This SRDP is also observed under -1 V pulses (Figure S12 (b)), with higher frequencies inducing more current changes. Such characteristics facilitate real-time learning by enabling synaptic weight modulation based on pulse frequency coding.

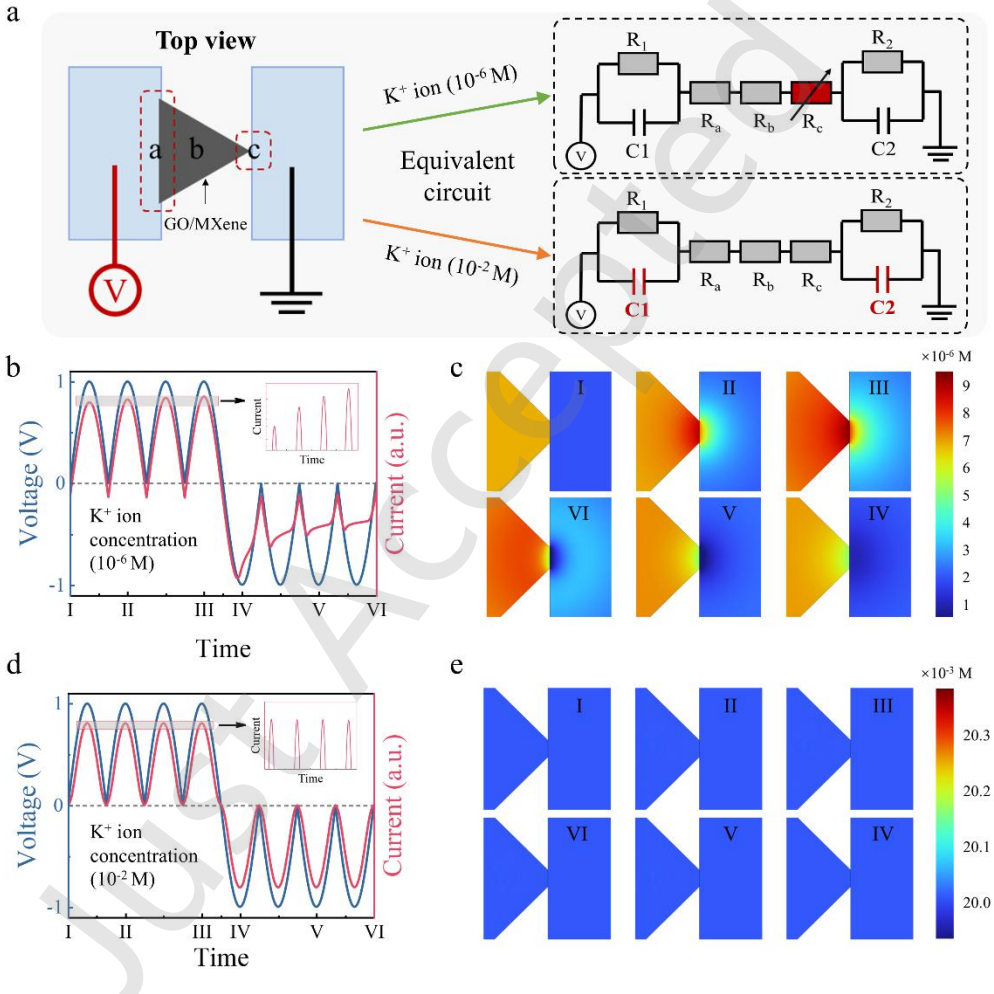

Figure 4. Mechanism of ion-concentration-modulated nanofluidic memristor. (a) Schematic illustration of nanofluidic memristor model (top-view geometry) and equivalent circuits at different ion concentrations. (b-c) Current curve and ion concentration distributions under low K^+ ionic concentration. (d-e) Current curves and ion concentration distributions under high K^+ ionic concentration.

To evaluate the influence of KCl concentration on synaptic short-term memory, we investigated PPF, PPD, SDDP, and SRDP under three different concentrations (10^{-6} M, 10^{-4} M, and 10^{-2} M). The PPF and PPD indices are both defined as the ratio of the response current of the second pulse to that of the first ($A_2/A_1 \times 100\%$). As shown in Figure 3g, both indices are generally higher in low-concentration solutions and exhibit a pronounced pulse-interval dependency, decaying slowly as the interval increases. In contrast, at the high concentration of 10^{-2} M, the correlation between the two pulses virtually vanishes when the interval exceeds 0.3 s. Figure 3h illustrates SDDP under different concentrations, defined as the ratio of the n-th pulse response current to the first ($A_n/A_1 \times 100\%$). The results indicate that spike-duration-dependent plasticity is observed only under low-concentration conditions, while high concentrations show minimal variation. Figure 3i shows SRDP under different concentrations, similary, it exhibits significant changes at low concentrations. In conclusion, the distinct behaviors of PPF, PPD, SDDP, and SRDP under three different K^+ concentrations demonstrate that the device can function as an on-demand switch for short-term memory via ion concentration modulation. This capability enables it to either

preserve temporal correlations for processing sequential information or to strip away temporal dependencies to handle transient events. To understand the mechanisms behind the memristive behavior and ion concentration sensitivity of the device, we performed simulations. DFT calculations confirm strong cation-π interactions between K^+ and the material, yielding binding energies of -2.55 eV and -6.59 eV for low (1 K^+) and high (3 K^+) concentrations, respectively. The stronger binding at high concentrations indicates that abundant K^+ ions act as energetic anchors, locking the interlayer spacing and accounting for the anti-swelling behavior observed in XRD analysis (Figure S9). Furthermore, the differential charge density analysis (Figure S13) clearly reveals a pronounced charge redistribution between the K+ ion and the substrate, providing direct visual evidence for the electron transfer during the cation-π interaction. we also performed simulations using COMSOL Multiphysics (The details in the Supporting Information). To simplify the computation, we adopted a two-dimensional model based on the device's top-view geometry, as shown in the left panel of Figure 4a (Figure S14). The model features a negatively charged GO/MXene thin film in the center, flanked by two rectangular solution pools containing KCl solutions of equal concentration. By applying an electrical signal to the right pool while grounding the left, we calculated the current-time (I-t) curves and ion concentration distributions. Based on the ion distribution profiles obtained at different concentrations (Figure S15), we represented the device using the equivalent circuit shown in the right panel of Figure 4a. In this model, the solution and electrode components are simplified as a parallel resistor and capacitor, while the thin film and its interfaces with the solution are modeled as three resistors. Because Figure S15 indicates that the ion concentration changes most significantly at the tip of the thin film, we focused our analysis on the dynamic ion concentration distribution in this tip region.

Figure 4b presents the calculated I-t and V-t curves, and Figure 4c shows the ion concentration distributions near the tip of the thin film in a low-concentration KCl solution (10^{-6} M). During the positive voltage sweep, the current peaks gradually increase as ions accumulate near the tip (see II and III); conversely, during the negative sweep, the current peaks decrease as ions deplete (see VI, V, and IV). Therefore, in the low-concentration solution, the equivalent resistance at the tip (R_c) acts as a variable resistor, and the memristive behavior and synaptic short-term memory primarily originate from changes in the ion concentration at the film tip. Figures 4d and e show the results for a high-concentration KCl solution (10^{-2} M). In this environment, the negative surface charge of the film is significantly shielded, reducing ion selectivity and preventing ion accumulation or depletion near the tip. Furthermore, the high background ion concentration masks subtle local changes. Consequently, the equivalent resistance (R_c) becomes a fixed resistor, eliminating memristive behavior and the temporal correlation of the signal is reduced. Instead, the device exhibits capacitive behavior dominated by the electric double-layer capacitance near the electrodes (Figure S15). The simulation results physically elucidate the regulation mechanism of ionic behavior in nanofluidic memristors. This ion-concentration-modulated synaptic plasticity is crucial for the future development of synaptic devices with environment-adaptive intelligent sensing capabilities. In biological systems, organisms dynamically adjust their behavioral patterns to adapt to their surrounding environment [12,50,51]. As illustrated in the predator-prey scenario in Figure 5a, the predator's nervous system can dynamically switch between processing temporal information and responding to transient events [52-54]: When a bat detects distant prey, its nervous system relies on temporal information to track the prey's movement and determine its trajectory, thereby enabling an accurate pursuit. However, when the bat approaches the prey and prepares to strike, to achieve high-precision real-time localization, the nervous system must switch to a transient signal processing mode to adapt to different hunting stage.

To demonstrate this scenario, we constructed a dynamic perception and recognition system with ion-gated modulation, as shown in Figure 5b. The moving prey was abstracted as a 2 × 2 pixel white block against a black background. Four consecutive spatiotemporal frames representing the prey's movement were sequentially input to an ion-sensitive 8 × 8 nanofluidic memristor array (where white pixels correspond to 1 V and black pixels to -1 V, software-assisted verification based on device experimental data). Leveraging the conductance changes induced by continuous pulse stimulation, the array processed the spatiotemporal information and integrated the four static frames into a single image containing spatiotemporal dynamic features. This image was then fed into a fully connected artificial neural network for motion direction learning and recognition. Thanks to the ion sensitivity of the nanofluidic memristor, we can modulate the conductance dynamics by regulating the internal ion concentration, which in turn dictates the processing of spatiotemporal information. As shown in Figure 5c, under a low concentration, 16 distinct input signals formed by continuous pulse sequences (0000 to 1111) are effectively converted into 16 different conductance states, meaning the device can precisely distinguish different input patterns. Figure S16 provides the details of the 16 different encoded test datasets. In contrast, under high concentration, these 16 inputs cannot be fully differentiated; the device's conductance relies solely on the last pulse, indicating that the device is capable of disengaging time dependence to address transient events. Figure 5d illustrates the consequence of this difference. At low concentrations, the device effectively retains the historical position of the moving object, producing a distinct motion "trail" (left panels), whereas at high concentrations, this historical information is virtually lost, and no trail is observed (right panels).

To further highlight the critical role of temporal correlation in motion tracking, we constructed a dataset for four motion directions (forward, backward, left, and right) by adding 10% salt-and-pepper noise (random black and white pixels). The dataset consisted of 80 sets (320 images in total) for training and 20 sets (80 images in total) for testing. We then performed training and testing over 500 epochs under both low and high concentration conditions. As shown in Figure 5e, the recognition accuracy reached 96.25% in the low-concentration solution and was only 33.25% in the high-concentration solution. Figures 5f and g present the confusion matrices for the recognition results under low and high concentrations, respectively, providing a detailed comparison between the predicted and true labels for the four motion directions. This system successfully demonstrates the influence of ion concentration on cognitive

function, indicating that ion-concentration-sensitive nanofluidic memristors offer a promising new approach for the construction of intelligent systems with advanced perception capabilities in the future.

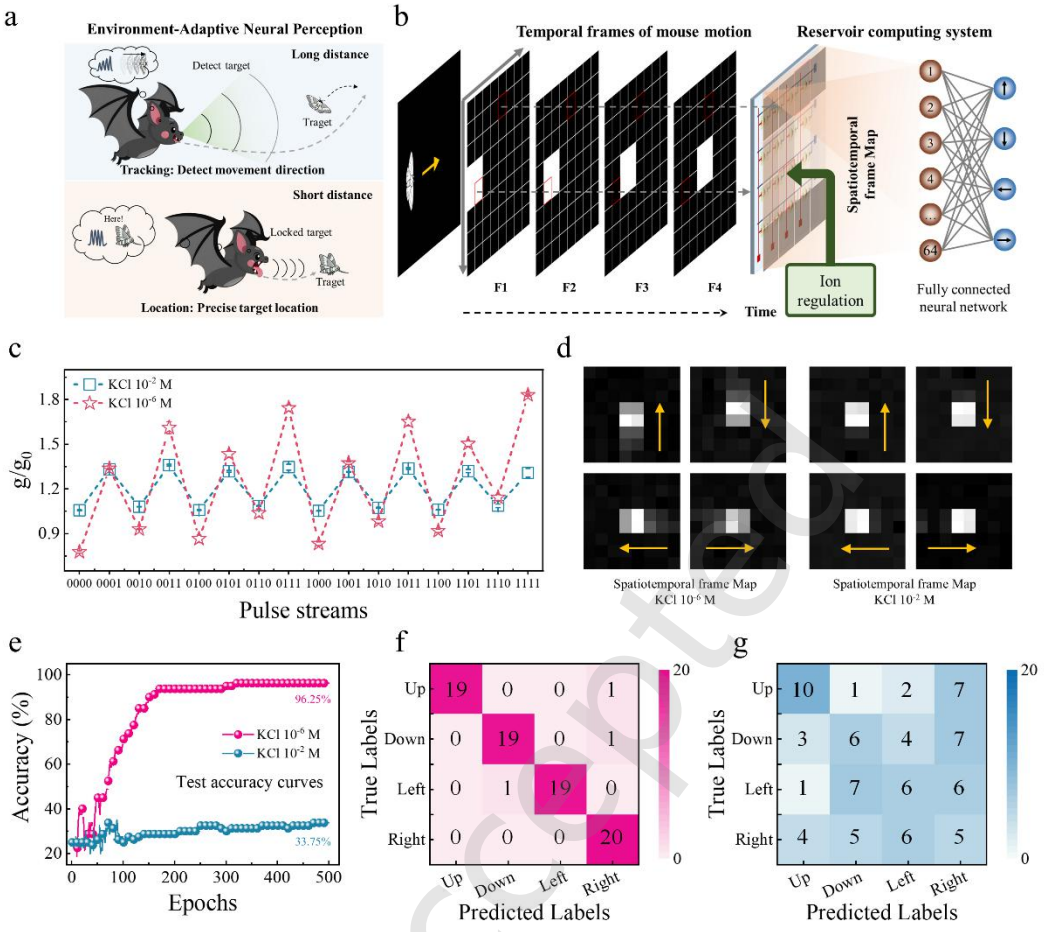

Figure 5. Simulation of bat dynamic hunting process with ion-concentration-modulated nanofluidic memristors. (a) Schematic illustration of the dynamic adjustment of temporal correlations in neural signals to adapt to different hunting stages. (b) Schematic of the motion direction recognition process. (c) g/g_0 values of 16 pulse streams under low (10^{-6} M) and high (10^{-2} M) ionic concentrations. (d) Spatiotemporal frame maps of four representative directions (up, down, left, and right) under low (10^{-6} M) and high (10^{-2} M) ion concentrations. (e) Test accuracy curves over 500 learning epochs at different ionic concentrations. Confusion matrices of recognition performance under (f) low and (g) high ionic concentrations

3. Conclusion

In conclusion, we developed an ion-concentration-modulated nanofluidic memristor featuring asymmetric nanochannels based on GO/MXene composites, which is capable of realizing K^+ ion concentration-dependent synaptic behavior via cation-π interactions. The device exhibits strong temporal correlation and typical biological synaptic plasticity, such as PPF, SDDP, and SRDP, at low K^+ ion concentrations, whereas these synaptic behaviors disappear at high concentrations, indicating a decrease in temporal correlation. The structural stability of a thin film in water (>40 d) is significantly enhanced by the Ti-O-C bonds formed between GO and MXene. A detailed comparison with other representative nanofluidic memristors is summarized in Table S1 (Supplementary Material). Compared to devices based on AAO, MoS2, or polymer membranes, our GO/MXene device exhibits long-term aqueous stability and a low operating voltage (~1 V), highlighting its unique potential for low-power bio-integrated applications. We successfully used the device to emulate the dynamic neural regulation of bats during the predation process, adapting to different hunting stages. These results offer a new strategy for the development of advanced functional neuromorphic devices by introducing ion concentration sensitivity for environment-adaptive dynamic perception

4. Experimental Section/Methods

Fabrication of asymmetric nanochannels: GO films and GO/MXene films were prepared by vacuum filtration over 48 hours and were air-dried naturally. To create the asymmetric structure, the freestanding films were processed using a UV laser marking machine. Specifically, the geometric patterns of the film were designed using computer software and imported into the laser marking machine. The film were then precisely cut according to the digital designs to obtain the asymmetric nanochannels. The detailed geometric parameters and patterns are illustrated in Figure S1 (c) in the Supplementary Material.

Device fabrication: The as-prepared films were immersed in the PDMS precursor and cured at 80 ℃ for 30 minutes to encapsulate the devices. After that, two reservoirs were made at the ends of the films. The fabrication method for a single device is reported in our previous paper. Detailed methods for preparing device arrays are described in the Supporting Information..

Electrical Measurements: The I-V curve was recorded with a Keysight B2912A sourcemeter unit. Before conducting measurements, the device was immersed in deionized water for approximately 4 hours to ensure conductivity. KCl solutions of

different concentrations were then added to two reservoirs. Two Ag/AgCl electrodes were inserted into the reservoirs to measure the current signals.

Electronic Supplementary Material: Supplementary material (additional experimental and calculation details) is available in the online version of this article at https://doi.org/10.26599/NR.2026.94909017.

Data availability

All data needed to support the conclusions in the paper are presented in the manuscript and the Electronic Supplementary Material. Additional data related to this paper may be requested from the corresponding author upon request."

Acknowledgements

This work was supported by the National Key Research and Development Program of China under Grant 2025YFF0520400, the NSFC for Distinguished Young Scholars (No. 52025022), the NSFC program (Nos. U23A20568, 52372137, 62571109, 52272140, 52402175), and the fund from Jilin Province (No. 20250101026JJ), and the fund from Changchun City (No. 25GNYZ75).

Declaration of competing interest

All the contributing authors report no conflict of interests in this work.

Author contribution statement

Z.Z.L., Y.L., and Z.Q.W. conceived the research idea. Z.Z.L. performed the simulations. Experiments with input from Z.Z.L. and M.Z.Z.. Z.Z.L, M.Z.Z., and Y.L. co-wrote the manuscript. Z.Q.W., Y.L., Y.T., X.Y.S., X.N.Z., H.Y.X., Y.C.L., supervised and coordinated the project.

Use of AI statement

None

References

[1] Yang, J. J.; Grollier, J.; Williams, R. S.; Huang, R. Neuromorphic Engineering: From Materials to Device Application. *Adv. Mater.* **2023**, 35, 2305078.

[2] Xia, Z.; Sun, X.; Wang, Z.; Meng, J.; Jin, B.; Wang, T. Low-Power Memristor for Neuromorphic Computing: From Materials to Applications. *Nano-Micro Lett.* **2025**, 17, 217.

[3] Aguirre, F.; Sebastian, A.; Le Gallo, M.; Song, W.; Wang, T.; Yang, J. J.; Lu, W.; Chang, M.-F.; Ielmini, D.; Yang, Y.; Mehonic, A.; Kenyon, A.; Villena, M. A.; Roldán, J. B.; Wu, Y.; Hsu, H.-H.; Raghavan, N.; Suñé, J.; Miranda, E.; Eltawil, A.; Setti, G.; Smagulova, K.; Salama, K. N.; Krestinskaya, O.; Yan, X.; Ang, K.-W.; Jain, S.; Li, S.; Alharbi, O.; Pazos, S.; Lanza, M. Hardware implementation of memristor-based artificial neural networks. *Nat. Commun.* **2024**, 15, 1974.

[4] Wang, Y.; Gou, S.; Dong, X.; Chen, X.; Wang, X.; Sun, Q.; Xia, Y.; Zhu, Y.; Zhang, Z.; Wang, D.; Zhang, J.; Guo, X.; Tong, L.; Ma, J.; Xu, Z.; Xie, Y.; Ma, S.; Zhou, P.; Chai, Y.; Bao, W. A biologically inspired artificial neuron with intrinsic plasticity based on monolayer molybdenum disulfide. *Nat. Electron.* **2025**, 8, 680–688.

[5] Janzakova, K.; Balafrej, I.; Kumar, A.; Garg, N.; Scholaert, C.; Rouat, J.; Drouin, D.; Coffinier, Y.; Pecqueur, S.; Alibart, F. Structural plasticity for neuromorphic networks with electropolymerized dendritic PEDOT connections. *Nat. Commun.* **2023**, 14, 8143.

[6] Senkowski, D.; Engel, A. K. Multi-timescale neural dynamics for multisensory integration. *Nat. Rev. Neurosci.* **2024**, 25, 625–642.

[7] Hongwei Tan; Yifan Zhou; Quanzheng Tao; Johanna Rosen; Sebastiaan van Dijken. Bioinspired multisensory neural network with crossmodal integration and recognition. *Nat. Commun.* **2021**, 12, 1120.

[8] Wang, W.; Jiang, Y.; Zhong, D.; Zhang, Z.; Choudhury, S.; Lai, J.-C.; Gong, H.; Niu, S.; Yan, X.; Zheng, Y.; Shih, C.-C.; Ning, R.; Lin, Q.; Li, D.; Kim, Y.-H.; Kim, J.; Wang, Y.-X.; Zhao, C.; Xu, C.; Ji, X.; Nishio, Y.; Lyu, H.; Tok, J. B.-H.; Bao, Z. Neuromorphic sensorimotor loop embodied by monolithically integrated, low-voltage, soft e-skin. *Science* **2023**, 380, 735–742.

[9] Wang, J.; Luo, Y.; Loh, X. J.; Chen, X. Integrated multimodal sensing for scent digitalization. *Matter* **2024**, 7, 2368–2381.

[10] Zhang, J.; Yao, H.; Mo, J.; Chen, S.; Xie, Y.; Ma, S.; Chen, R.; Luo, T.; Ling, W.; Qin, L.; Wang, Z.; Zhou, W. Finger-inspired rigid-soft hybrid tactile sensor with superior sensitivity at high frequency. *Nat. Commun.* **2022**, 13, 5076.

[11] Wu, Z.; Lu, J.; Shi, T.; Zhao, X.; Zhang, X.; Yang, Y.; Wu, F.; Li, Y.; Liu, Q.; Liu, M. A Habituation Sensory Nervous System with Memristors. *Adv. Mater.* **2020**, 32, 2004398.

[12] Shi, J.; Lin, Y.; Wang, Z.; Shan, X.; Tao, Y.; Zhao, X.; Xu, H.; Liu, Y. Adaptive Processing Enabled by Sodium Alginate Based Complementary Memristor for Neuromorphic Sensory System. *Adv. Mater.* **2024**, 36, 2314156.

[13] Benda, J. Neural adaptation. *Curr. Biol.* **2021**, 31, R110–R116.

[14] Bruno, U.; Rana, D.; Ausilio, C.; Mariano, A.; Bettucci, O.; Musall, S.; Lubrano, C.; Santoro, F. An organic brain-inspired platform with neurotransmitter closed-loop control, actuation and reinforcement learning. *Mater. Horiz.* **2024**, 11, 2865–2874.

[15] Harikesh, P. C.; Yang, C.-Y.; Tu, D.; Gerasimov, J. Y.; Dar, A. M.; Armada-Moreira, A.; Massetti, M.; Kroon, R.; Bliman, D.; Olsson, R.; Stavrinidou, E.; Berggren, M.; Fabiano, S. Organic electrochemical neurons and synapses with ion mediated spiking. *Nat. Commun.* **2022**, 13, 901.

[16] Ling, Y.; Yu, L.; Guo, Z.; Bian, F.; Wang, Y.; Wang, X.; Hou, Y.; Hou, X. Single-Pore Nanofluidic Logic Memristor with Reconfigurable Synaptic Functions and Designable Combinations. *J. Am. Chem. Soc.* **2024**, 146, 14558–14565.

[17] Liu, X.; Li, X.; Shen, P.; Cong, B.; Wang, L. Fundamental role of brain-organ interaction in behavior-driven holistic homeostasis. *Fundam. Res.* **2025**, 5, 2626–2638.

[18] Yang, L.; Ni, Y.; Jiang, C.; Liu, L.; Zhang, S.; Liu, J.; Sun, L.; Xu, W. A neuromorphic device mimicking synaptic plasticity under different body fluid K+ homeostasis for artificial reflex path construction and pattern recognition. *Fundam. Res.* **2024**, 4, 353–361.

[19] Ding, F.; O'Donnell, J.; Xu, Q.; Kang, N.; Goldman, N.; Nedergaard, M. Changes in the composition of brain interstitial ions control the sleep-wake cycle. *Sci.* **2016**, 352, 550–555.

[20] Nordentoft, M. S.; Takahashi, N.; Heltberg, M. S.; Jensen, M. H.; Rasmussen, R. N.; Papoutsi, A. Local changes in potassium ions regulate input integration in active dendrites. *PLoS Biol.* **2024**, 22, e3002935.

[21] Sourisse, J. M.; Tabarova, M.; Romeo, D.; Kam, Y. C.; Schunter, C. Acidification alters anxiety-like behaviour and brain gene expression in zebrafish. *Sci. Total Environ.* **2025**, 987, 179822.

[22] Tang, R.-J.; Zhao, F.-G.; Yang, Y.; Wang, C.; Li, K.; Kleist, T. J.; Lemaux, P. G.; Luan, S. A calcium signalling network activates vacuolar K+ remobilization to enable plant adaptation to low-K environments. *Nat. Plants* **2020**, 6, 384–393.

[23] Zhang, S.; Zhu, J.; Qiu, R.; Liu, D.; Ren, Q.; Zhang, M. Flexible Tunable-Plasticity Synaptic Transistors for Mimicking Dynamic Cognition and Reservoir Computing. *Adv. Mater.* **2025**, 37, 2418418.

[24] Deisseroth, K. From microbial membrane proteins to the mysteries of emotion. *Cell* **2021**, 184, 5279–5285.

[25] Seifter, J. L. Body Fluid Compartments, Cell Membrane Ion Transport, Electrolyte Concentrations, and Acid-Base Balance. *Semin. Nephrol.* **2019**, 39, 368–379.

[26] Ye Qiu; Chengjun Wang; Xiaoyan Lu; Huaping Wu; Xiaolong Ma; Jiahui Hu; Hangcheng Qi; Ye Tian; Zheng Zhang; Guanjun Bao; Hao Chai; Jizhou Song; Aiping Liu. A Biomimetic Drosera Capensis with Adaptive Decision-Predation Behavior Based on Multifunctional Sensing and Fast Actuating Capability. *Adv. Funct. Mater.* **2022**, 32, 2110296.

[27] Huang, M.; Xu, L.; del Alamo, J. A.; Li, J.; Yildiz, B. Nonlinear Ion Dynamics Enable Spike Timing Dependent Plasticity of Electrochemical Ionic Synapses. *Adv. Mater.* **2025**, 37, 2418484.

[28] Alfonsa, H.; Chakrabarty, A.; Vyazovskiy, V. V.; Akerman, C. J. Sleep-wake-related changes in intracellular chloride regulate plasticity at glutamatergic cortical synapses. *Curr. Biol.* **2025**, 35, 1373-1381.e3.

[29] Romele, P.; Gkoupidenis, P.; Koutsouras, D. A.; Lieberth, K.; Kovács-Vajna, Z. M.; Blom, P. W. M.; Torricelli, F. Multiscale real time and high sensitivity ion detection with complementary organic electrochemical transistors amplifier. *Nat. Commun.* **2020**, 11, 3743.

[30] Li, J.; Zhao, W.; Fu, C.; Zhai, Z.; Xu, P.; Diao, X.; Guo, W.; Yin, J. An ion-electronic hybrid artificial neuron with a widely tunable frequency. *Nat. Commun.* **2025**, 16, 7911.

[31] Li, P.; Bräuniger, Y.; Kunigkeit, J.; Zhou, H.; Ortega Vega, M. R.; Zhang, E.; Grothe, J.; Brunner, E.; Kaskel, S. Bioactive Ion-Based Switchable Supercapacitors. *Angew. Chem. Int. Ed.* **2022**, 61,

e202212250.
[32] Panigrahi, D.; Zucchelli, D.; Hamid, Z.; Kousseff, C.; Sarkar, A.; Pavlou, A.; Ling, Z.; Kashani, S.; McCulloch, I.; Blom, P. W. M.; Torricelli, F.; Gkoupidenis, P. Ion-Reconfigurable "N"-Shaped Antiambipolar Behavior in Organic Electrochemical Transistors. *Adv. Mater.* e16684.
[33] Emmerich, T.; Ronceray, N.; Agrawal, K. V.; Garaj, S.; Kumar, M.; Noy, A.; Radenovic, A. Nanofluidics. *Nat. Rev. Methods Primers* **2024**, 4, 69.
[34] Hou, Y.; Ling, Y.; Wang, Y.; Wang, M.; Chen, Y.; Li, X.; Hou, X. Learning from the Brain: Bioinspired Nanofluidics. *J. Phys. Chem. Lett.* **2023**, 14, 2891–2900.
[35] Yu, L.; Li, X.; Luo, C.; Lei, Z.; Wang, Y.; Hou, Y.; Wang, M.; Hou, X. Bioinspired nanofluidic iontronics for brain-like computing. *Nano Res.* **2023**, 17, 503–514.
[36] Zhang, M.; Xu, G.; Zhang, H.; Xiao, K. Nanofluidic Volatile Threshold Switching Ionic Memristor: A Perspective. *ACS Nano* **2025**, 19, 10589–10598.
[37] Cui, Y.; Gao, L.; Ying, C.; Tian, J.; Liu, Z. Two-Dimensional Material-Based Nanofluidic Devices and Their Applications. *ACS Nano* **2025**, 19, 1911–1943.
[38] Tang, P.; Qiu, Z.; Zhu, Y.; Liu, K.; Luo, Z.; Jing, P.; Tao, Z.; Lao, Y.; Xie, S.; Ye, C.; Zhu, J.; Liu, Y.; Dou, Q.; Yan, X. A Zinc Ion Capacitor-Based Fluidic Memristor. *Adv. Mater.* **2025**, e12592.
[39] Xiao, Y.; Sun, W.; Gao, C.; Jin, J.; Siraj, M.; Yan, P.; Sun, F.; Zhang, X.; Wang, Q.; Huang, W.; Sheng, C.; Yu, Y. F. Neural Functions Enabled by a Polarity-Switchable Nanofluidic Memristor. *Nano Lett.* **2024**, 24, 12515–12521.
[40] Li, Z.; Lin, Y.; Shan, X.; Wang, Z.; Zhao, X.; Tao, Y.; Xu, H.; Liu, Y. Optogenetics-Inspired Nanofluidic Artificial Dendrite with Spatiotemporal Integration Functions. *Adv. Mater.* **2025**, 37, 2502438.
[41] Xiong, T.; Li, C.; He, X.; Xie, B.; Zong, J.; Jiang, Y.; Ma, W.; Wu, F.; Fei, J.; Yu, P.; Mao, L. Neuromorphic functions with a polyelectrolyte-confined fluidic memristor. *Sci.* **2023**, 379, 156–161.
[42] Xu, Y.-T.; Yu, S.-Y.; Li, Z.; Kou, B.-H.; Pang, J.-X.; Zhao, W.-W.; Chen, H.-Y.; Xu, J.-J. A nanofluidic spiking synapse. *Proc. Natl. Acad. Sci.* **2024**, 121, e2403143121.
[43] Pillai, E. K.; Franze, K. Mechanics in the nervous system: From development to disease. *Neuron* **2024**, 112, 342–361.
[44] Nguyen, H.; Glaaser, I. W.; Slesinger, P. A. Direct modulation of G protein-gated inwardly rectifying potassium (GIRK) channels. *Front. Physiol.* **2024**, 15, 1386645.
[45] Bellot-Saez, A.; Kékesi, O.; Morley, J. W.; Buskila, Y. Astrocytic modulation of neuronal excitability through K+ spatial buffering. *Neurosci. Biobehav. Rev.* **2017**, 77, 87–97.
[46] Contreras, S. A.; Schleimer, J.-H.; Gulledge, A. T.; Schreiber, S. Activity-mediated accumulation of potassium induces a switch in firing pattern and neuronal excitability type. *PLoS Comput. Biol.* **2021**, 17, e1008510.
[47] Yang, J.; Li, M.; Fang, S.; Wang, Y.; He, H.; Wang, C.; Zhang, Z.; Yuan, B.; Jiang, L.; Baughman, R. H.; Cheng, Q. Water-induced strong isotropic MXene-bridged graphene sheets for electrochemical energy storage. *Sci.* **2024**, 383, 771–777.
[48] Kumar, P. V.; Bardhan, N. M.; Tongay, S.; Wu, J.; Belcher, A. M.; Grossman, J. C. Scalable enhancement of graphene oxide properties by thermally driven phase transformation. *Nat. Chem.* **2014**, 6, 151–158.
[49] Chen, L.; Shi, G.; Shen, J.; Peng, B.; Zhang, B.; Wang, Y.; Bian, F.; Wang, J.; Li, D.; Qian, Z.; Xu, G.; Liu, G.; Zeng, J.; Zhang, L.; Yang, Y.; Zhou, G.; Wu, M.; Jin, W.; Li, J.; Fang, H. Ion sieving in graphene oxide membranes via cationic control of interlayer spacing. *Nat.* **2017**, 550, 380–383.
[50] Cheng, Y.; Zhang, J.; Lin, Y.; Wang, Z.; Shan, X.; Tao, Y.; Zhao, X.; Xu, H.; Liu, Y. Bioinspired Adaptive Neuron Enabled by Self‐powered Optoelectronic Memristor and Threshold Switching Memory for Neuromorphic Visual System. *Adv. Sci.* **2025**, 12, 2417461.
[51] Wang, S.; Gao, S.; Tang, C.; Occhipinti, E.; Li, C.; Wang, S.; Wang, J.; Zhao, H.; Hu, G.; Nathan, A.; Dahiya, R.; Occhipinti, L. G. Memristor-based adaptive neuromorphic perception in unstructured environments. *Nat. Commun.* **2024**, 15, 4671.
[52] Tseng, Y.-T.; Schaefke, B.; Wei, P.; Wang, L. Defensive responses: behaviour, the brain and the body. *Nat. Rev. Neurosci.* **2023**, 24, 655–671.
[53] Nishiumi, N.; Fujioka, E.; Hiryu, S. Bats integrate multiple echolocation and flight tactics to track prey. *Curr. Biol.* **2024**, 34, 2948-2956.e6.
[54] Ghose, K.; Horiuchi, T. K.; Krishnaprasad, P. S.; Moss, C. F. Echolocating Bats Use a Nearly Time-Optimal Strategy to Intercept Prey. *PLoS Biol.* **2006**, 4, e108.

Electronic Supplementary Material

Bioinspired ion-concentration-modulated nanofluidic memristor for environment-adaptive dynamic perception

Zhuangzhuang Li, Mingzhe Zhang, Ya Lin, Xuanyu Shan, Ye Tao, Xiaoning Zhao, Zhongqiang Wang, Haiyang Xu, and Yichun Liu

State Ley Laboratory of Integrated Optoelectronics, Key Laboratory for UV Light-Emitting Materials and Technology of Ministry of Education, School of Physics, Northeast Normal University, 5268 Renmin Street, Changchun, China

Supporting information to https://doi.org/10.26599/NR.2026.94909017

1. Simulation:

The ions distribution and I-t curves was performed using COMSOL Multiphysics. Under the condition of working temperature of 293.15K, a two-dimensional geometric model was used in this simulation as shown in Figure S11. A and B represent the length and width of the solution reservoirs, respectively, which are 10 mm and 5 mm. L (3 mm) is the height of the trapezoidal film. D1 and D2 are the long and short sides of the trapezoidal film, corresponding to 6mm and 0.1mm respectively. A sinusoidal voltage signal with an amplitude of 1 V and a period of 20 s is applied to the long side of the solution reservoir on the right. The long side of the left solution reservoir is grounded. The Nernst-Planck equation was used to caculated the ions distribution.

$$J_i = -D_i \nabla c_i - \frac{z_i F}{RT} c_i \nabla \phi$$

This equation consists of two parts, $-D_i \nabla c_i$ describes the diffusion of ions under a concentration gradient, while $-\frac{z_i F}{RT} c_i \nabla \phi$ describes the migration of ions under the influence of an electric field. Among them, J_i is the flux of ion i, and D_i, c_i are the diffusion coefficient and the concentration of ion i. z_i, F, R, T, and ϕ are the charge number of ionic species i, Faraday's constant (approximately 96485 C/mol), gas constant, temperature, and electrical potential [1-3].

The Poisson equation describes the relationship between electric field and charge density.

$$\nabla^2 \phi = \frac{F^2}{\varepsilon RT}(c_- - c_+)$$

Where ε is dielectric constant, c_- and c_+ represent the concentration of anions and cations respectively [4].

Multi-physics field coupling studies were conducted to simulate the spatial distribution of ions at different time points under sinusoidal voltage scanning conditions.

2. Supplementary Figures

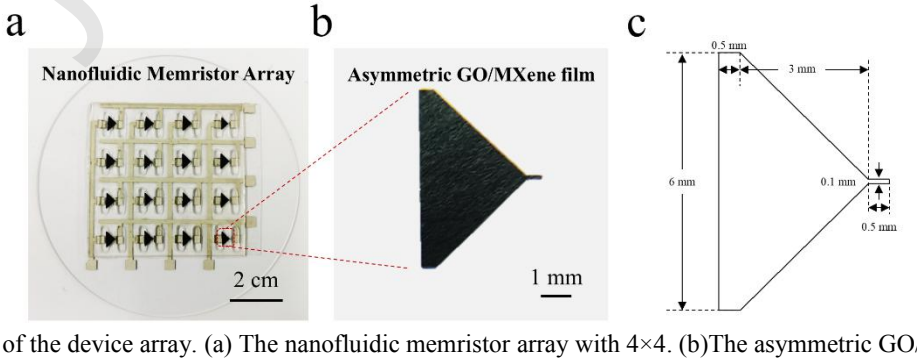

Figure S1. Photograph of the device array. (a) The nanofluidic memristor array with 4×4. (b)The asymmetric GO/Mxene film. (c) The detailed geometric parameters and patterns.

Address correspondence to Ya Lin, liny474@nenu.edu.cn; Ye Tao, taoy506@nenu.edu.cn; Zhongqiang Wang, wangzq752@nenu.edu.cn

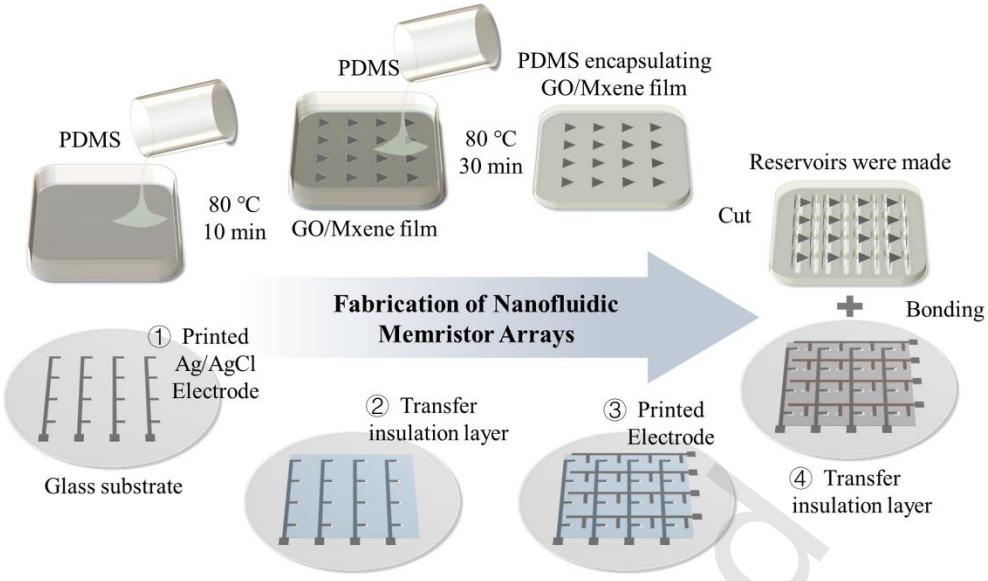

Figure S2. Schematic diagram of the fabrication method for nanofluidic memrsitor array. The upper section demonstrates the fabrication method for the nanochannels and solution reservoirs of nanofluidic memristor, while the lower section illustrates the electrode fabrication method for the array.

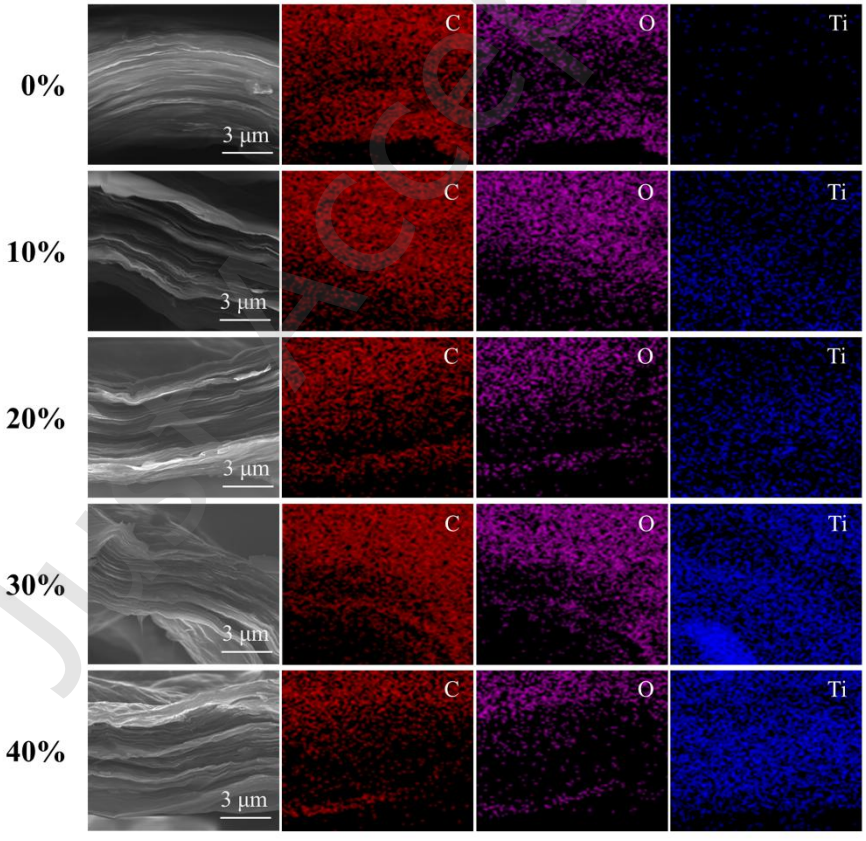

Figure S3. SEM cross-sectional images and EDX mapping for C, O, and Ti of GO/MXene composite films with varying MXene contents (rang from 0 to 40%).

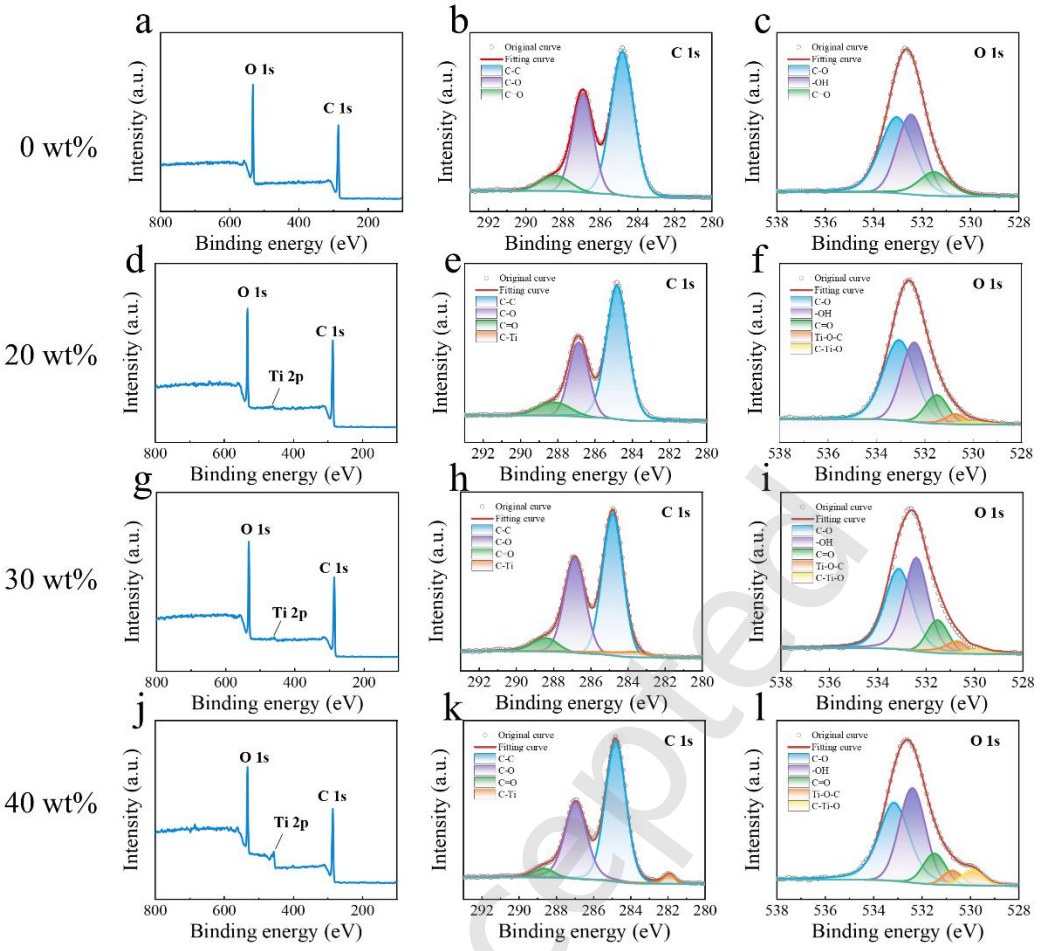

Figure S4. XPS spectra of differet GO/MXene composite films. (a, d, g, j) XPS survey scan spectrum of the GO/MXene composite films. (b, e, h, k) XPS spectra of C 1s of different GO/MXene composite films. (c, f, i, l) Component peak fitting of the XPS spectrum for O 1s.

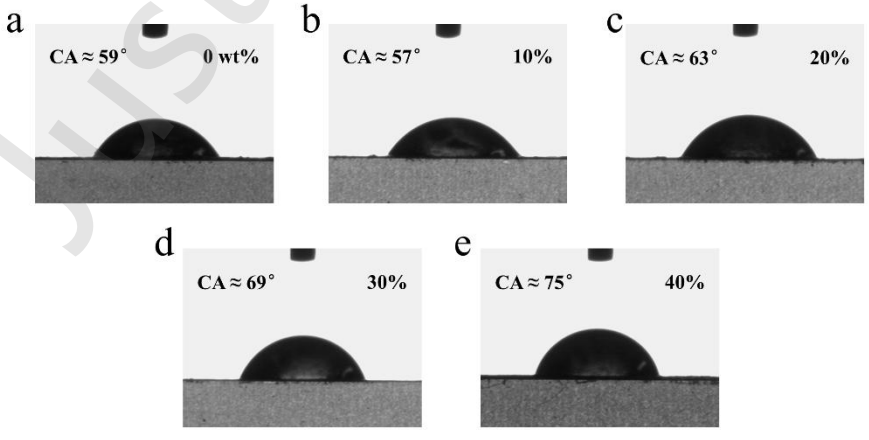

Figure S5. The contact angles of GO/MXene composite films with MXene contents of (a) 0 wt%, (b) 10 wt%, (c) 20 wt%, (d) 30 wt%, and (e) 40 wt% MXene content are approximately 59°, 57°, 63°, 69°, and 75°, respectively.

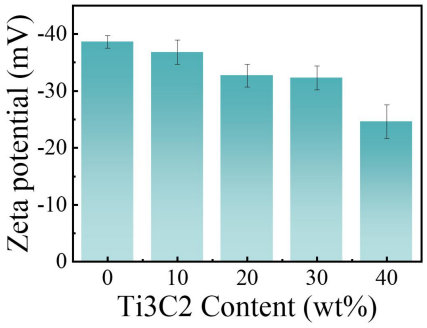

Figure S6. Zeta potential of GO/MXene dispersions with MXene contents ranging from 0 wt% to 40 wt%.

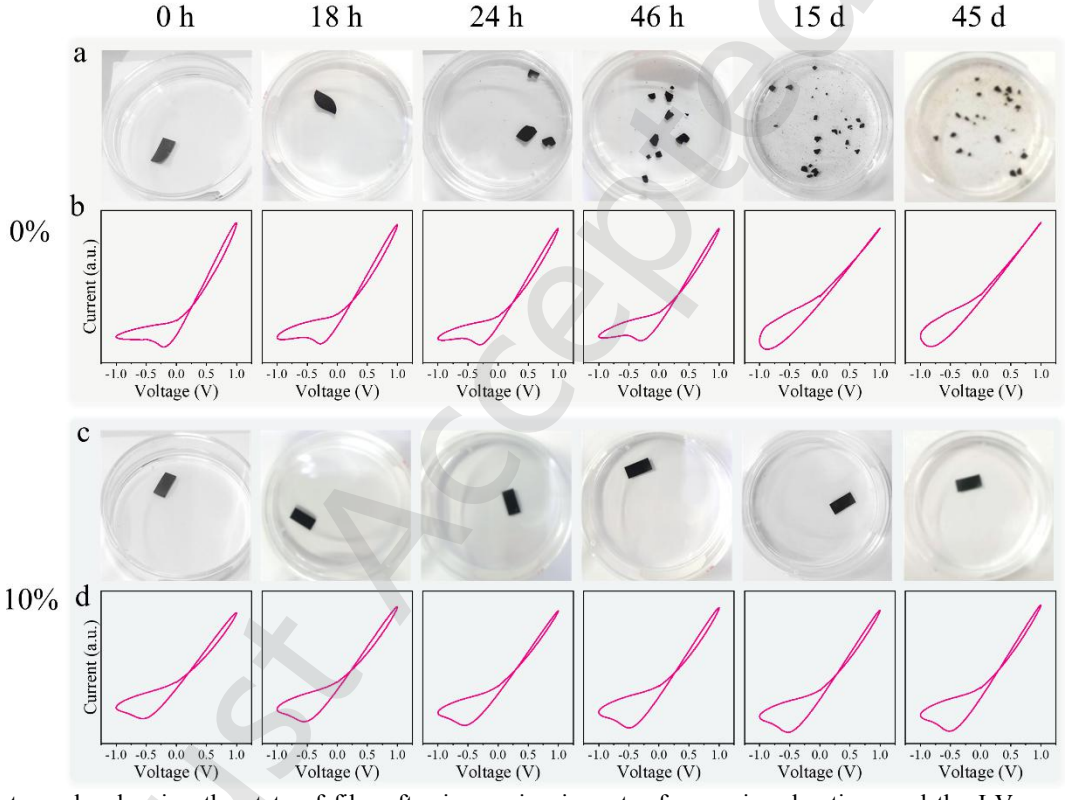

Figure S7. Photographs showing the state of film after immersion in water for varying durations and the I-V curves showing the corresponding memristive characteristic. (a, b) For the pure GO device, despite the visible film rupture after 24h, the PDMS encapsulation initially preserved the device structure, allowing memristive behavoir to persist to 46 h. However, after 15 days, the complete dispersion of the GO film destroyed the conductive path, resulting in the loss of memristive characteristics. (c. d) The 10 wt% GO/MXene device retained stable I-V hysteresis loops throughout the 45-day test, confirming the critical role of MXene in enhancing both structural and electrical stability.

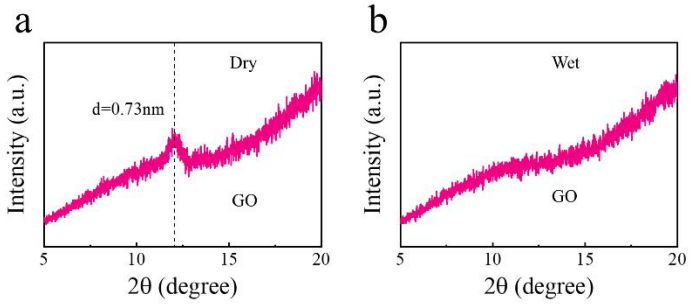

Figure S8. XRD diffraction pattern of layered GO films. (a) XRD analysis of the dried film shows a characteristic peak corresponding to an interlayer spacing of approximately 0.73nm (b) The XRD peaks of the film disappeared after it became damp due to water immersion. This indicates that the increased interlayer spacing caused the peak positions to shift below 5°, placing them outside the measurable range.

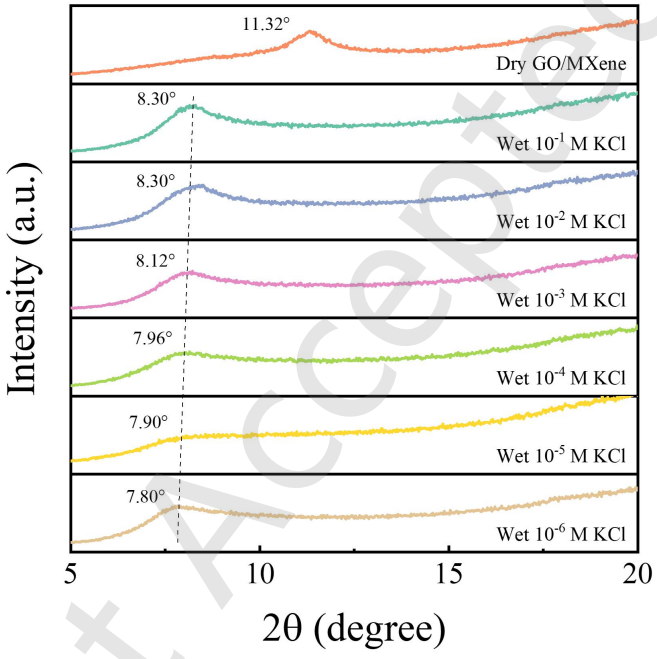

Figure S9. XRD diffraction pattern of layered GO/MXene films immersed in KCl solutions of different concentrations. as the KCl concentration increased, the diffraction angle shifted slightly to higher values, which implies that the increase in interlayer spacing becomes smaller at higher salt concentrations. This phenomenon can be explained by the cation-π interactions between the potassium ions and the aromatic regions of the GO/MXene sheets [5].

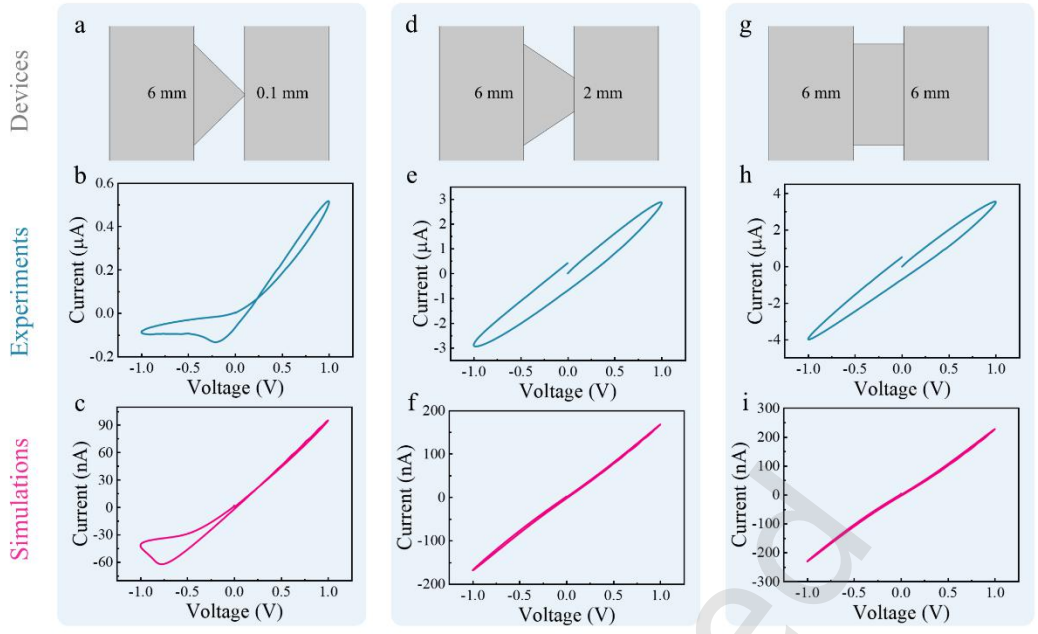

Figure S10. The experiment and simulation results for the device with narrow sides of (a-c) 0.1 mm, (d-f) 2 mm, and (g-i) 6 mm.

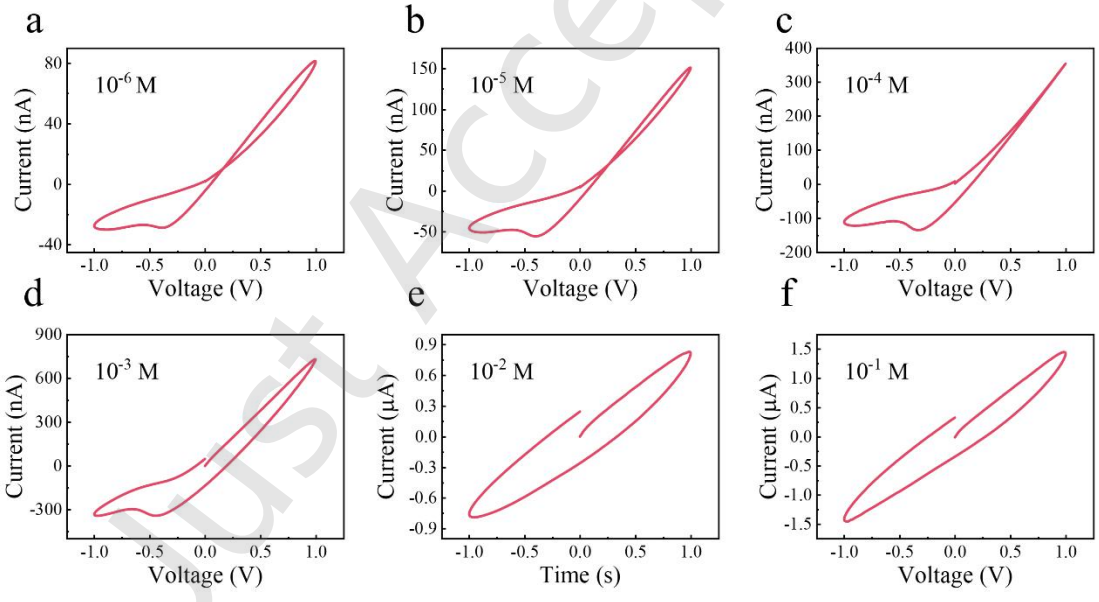

Figure S11. I-V curves for KCl solutions with concentrations ranging from (a) 10^{-6} M to (f) 10^{-1} M

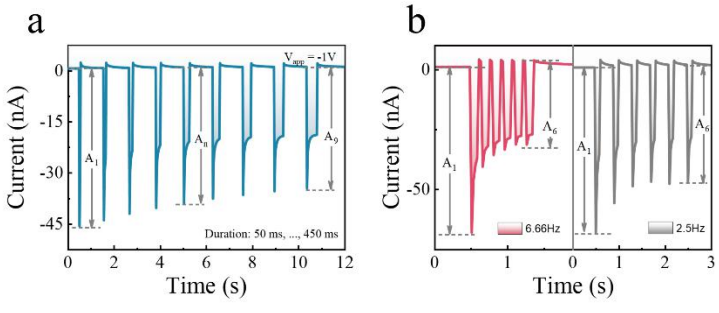

Figure S12. (a) SDDP functions triggered by various pulses with an amplitude of -1 V and widths ranging from 50 to 450 ms. (b)

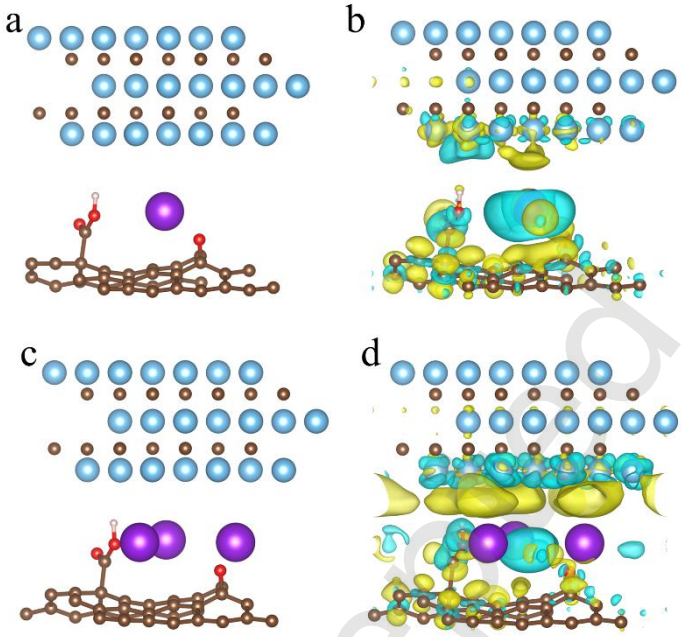

Figure S13. DFT calculations verifying the cation-π interactions at different concentrations. (a) Optimized structural model of 1 K^+ ion adsorbed on the material substrate, representing low concentration. (b) Corresponding differential charge density distribution of (a), showing the charge transfer between K^+ and the substrate. (c) Optimized structural model of 3 K^+ ions adsorbed on the material substrate, representing high concentration. (d) Corresponding differential charge density distribution of (c). Yellow and blue surfaces represent charge accumulation and depletion, respectively.

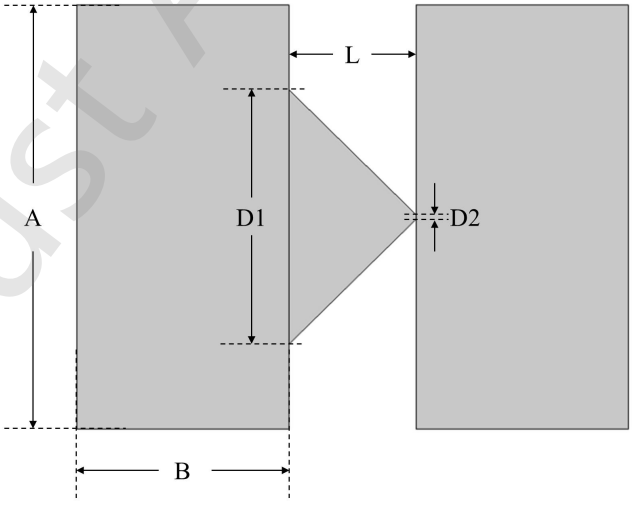

Figure S14. A two-dimensional geometric model of nanofluidic memristor. A = 10 mm, B = 5 mm, D1 = 6 mm, D2 = 0.1 mm, and L = 3 mm.

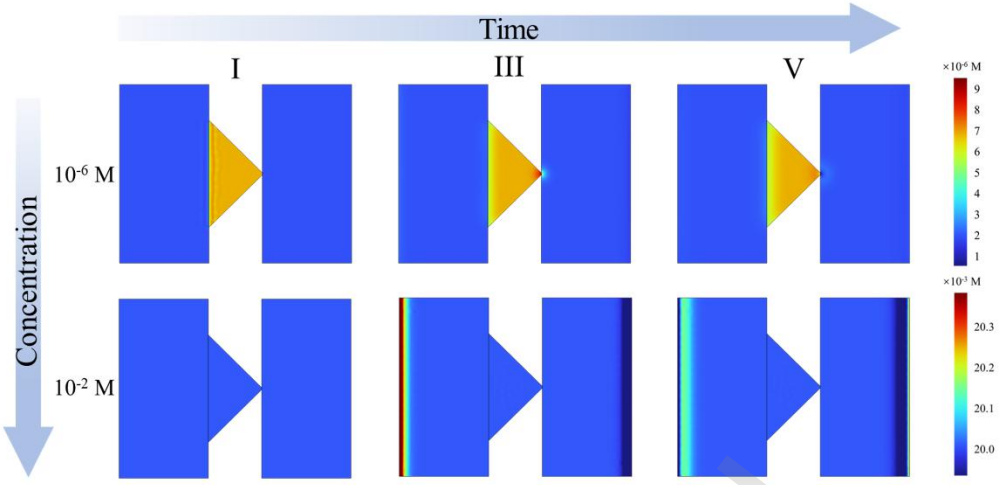

Figure S15. The ions distribution profiles at various concentrations and time points.

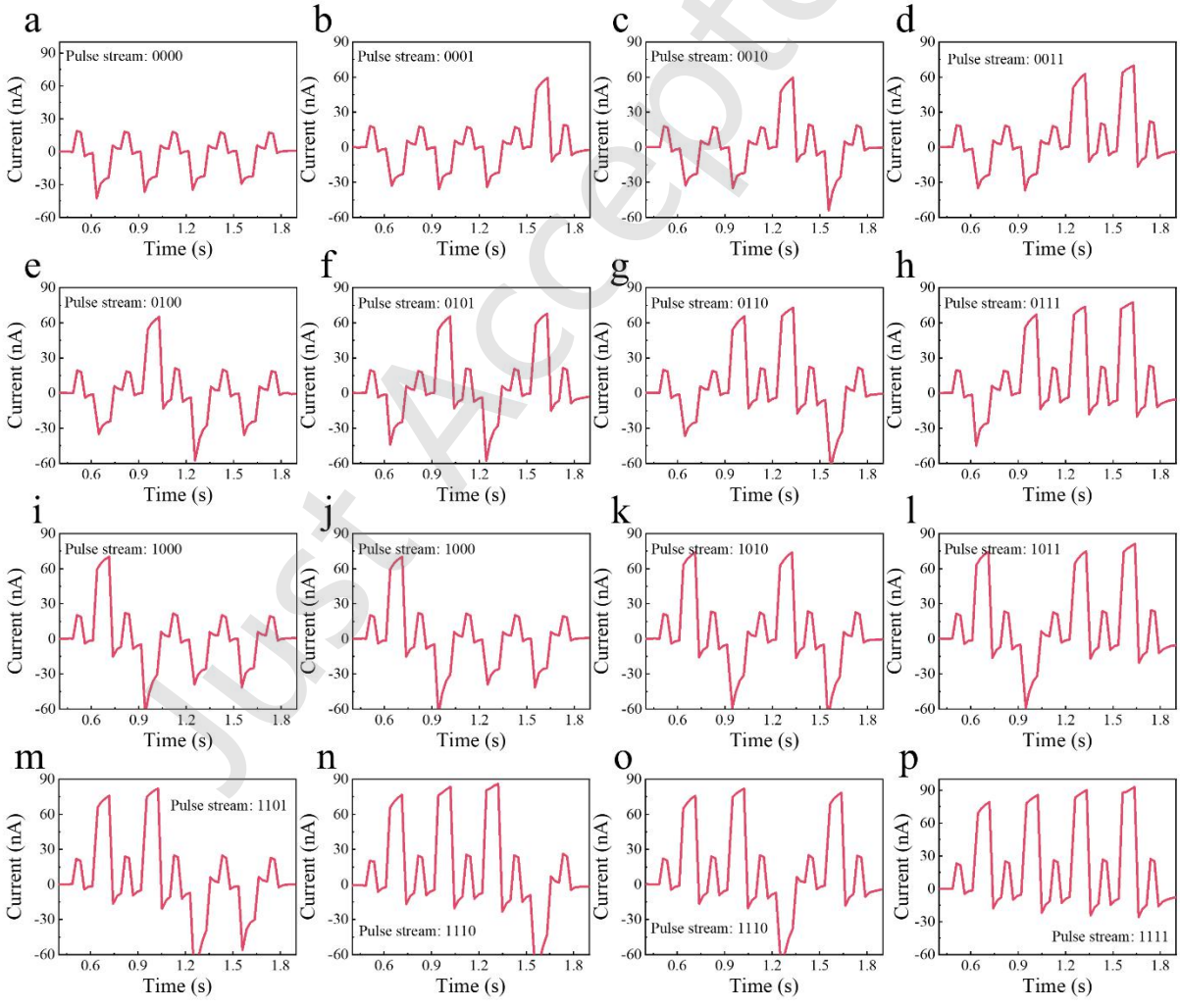

Figure S16. Current response under 16 different pulse sequences. (a) 0000, (b) 0001, (c) 0010, (d) 0011, (e) 0100, (f) 0101, (g) 0110, (h) 0111, (i) 1000, (j) 1001, (k) 1010, (l) 1011, (m) 1100, (n) 1101, (o) 1110, (p) 1111.

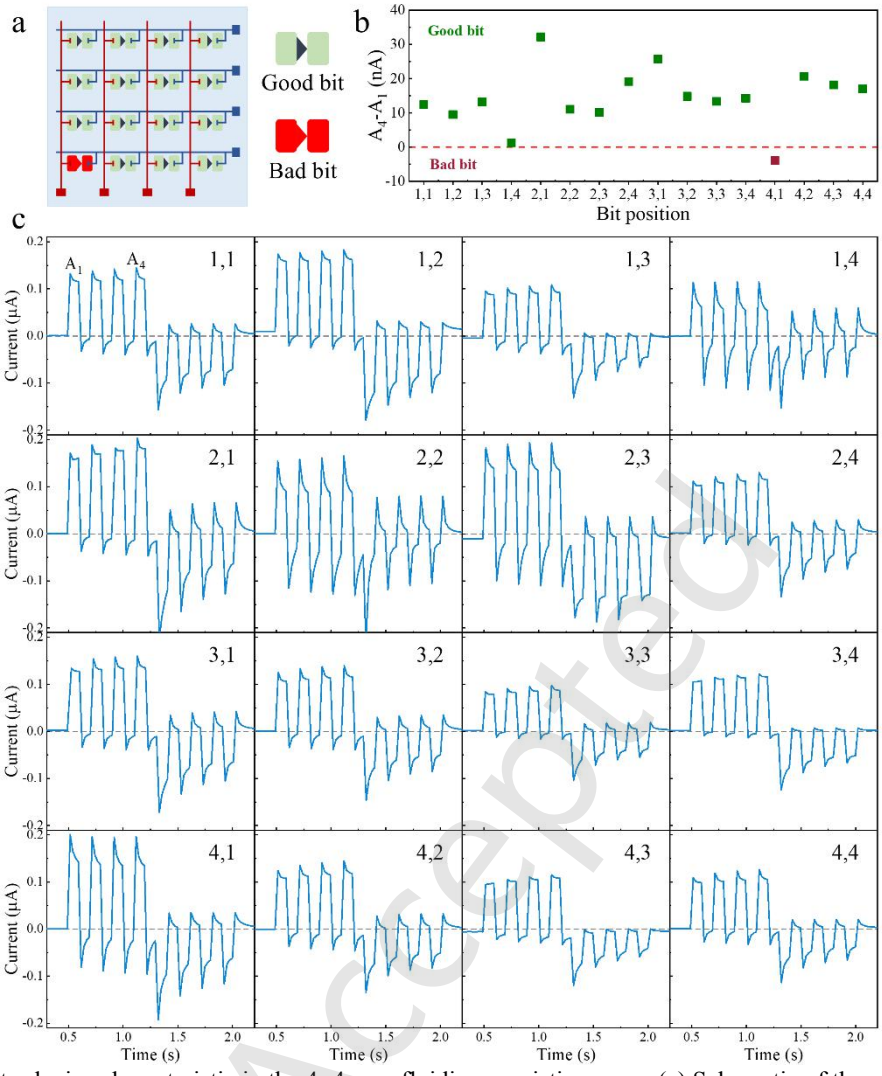

Figure S17. The device-to-device characteristic in the 4×4 nanofluidic memristive array. (a) Schematic of the nanofluidic memristive array. The red represents "bad bits" and the green represents "good bits". (b) The current difference is used to evaluate the quality of the device. (c) The current-time curves of the device under the electrical pulse mode.

3. Supplementary tables

Table S1. Comparison of operating voltage, aqueous stability, and ion sensitivity between this work and existing nanofluidic memristors based on AAO, MoS2, and polymers.

Ref.	Material System	Operating Voltage (V)	Aqueous Stability	Ion sensitivity
[6]	Poly-L-lysine (PLL)	10	---	PH sensitivity
[7]	MoS2 & Graphene	1	---	---
[8]	PimB	1	---	Chemical-electric signal transduction
[9]	Nanoparticles	5	---	---
[10]	PEODT: PSS membrane	1	---	Neurochemicals
[11]	Anodized aluminum oxide (AAO)	10	---	Electrolyte concentration
[12]	PDMS-glass	5	---	---
[13]	PET	2	---	Ion concentration
This work	GO/MXene	1	> 40 days	Ion concentration

3. Supplementary References

[1] Kamsma, T. M.; Boon, W. Q.; Spitoni, C.; van Roij, R. Unveiling the capabilities of bipolar conical channels in neuromorphic iontronics. Faraday Discuss. **2023**, 246, 125–140.

[2] Javier Cervera; Birgitta Schiedt; Reinhard Neumann; Salvador Mafé; Patricio Ramírez. Ionic conduction, rectification, and selectivity in single conical nanopores. J. Chem. Phys. **2006**, 124, 104706.

[3] Cervera, J.; Schiedt, B.; Ramírez, P. A Poisson/Nernst-Planck model for ionic transport through synthetic conical nanopores. EPL-EUROPHYS LETT **2005**, 71, 35–41.

[4] Li, H.; Lu, B. An ionic concentration and size dependent dielectric permittivity Poisson-Boltzmann model for biomolecular solvation studies. J. Chem. Phys. **2014**, 141, 024115

[5] Chen, L.; Shi, G.; Shen, J.; Peng, B.; Zhang, B.; Wang, Y.; Bian, F.; Wang, J.; Li, D.; Qian, Z.; Xu, G.; Liu, G.; Zeng, J.; Zhang, L.; Yang, Y.; Zhou, G.; Wu, M.; Jin, W.; Li, J.; Fang, H. Ion sieving in graphene oxide membranes via cationic control of interlayer spacing. Nature 2017, 550, 380–383.

[6] Shi, D.; Wang, W.; Liang, Y.; Duan, L.; Du, G.; Xie, Y. Ultralow energy consumption angstrom-fluidic memristor. Nano Lett. 2023, 23, 11662–11668.

[7] P. Robin; T. Emmerich; A. Ismail; A. Niguès; Y. You; G.-H. Nam; A. Keerthi; A. Siria; A. K. Geim; B. Radha; L. Bocquet. Long-term memory and synapse-like dynamics in two-dimensional nanofluidic channels. Science 2023, 379, 161–167.

[8] Xiong, T.; Li, C.; He, X.; Xie, B.; Zong, J.; Jiang, Y.; Ma, W.; Wu, F.; Fei, J.; Yu, P.; Mao, L. Neuromorphic functions with a polyelectrolyte-confined fluidic memristor. Science 2023, 379, 156–161.

[9] Kamsma, T. M.; Kim, J.; Kim, K.; Boon, W. Q.; Spitoni, C.; Park, J.; Van Roij, R. Brain-inspired computing with fluidic iontronic nanochannels. Proc. Natl. Acad. Sci. 2024, 121, e2320242121.

[10] Xu, Y.-T.; Yu, S.-Y.; Li, Z.; Kou, B.-H.; Pang, J.-X.; Zhao, W.-W.; Chen, H.-Y.; Xu, J.-J. A nanofluidic spiking synapse. Proc. Natl. Acad. Sci. 2024, 121, e2403143121.

[11] Xiao, Y.; Sun, W.; Gao, C.; Jin, J.; Siraj, M.; Yan, P.; Sun, F.; Zhang, X.; Wang, Q.; Huang, W.; Sheng, C.; Yu, Y. F. Neural Functions Enabled by a Polarity-Switchable Nanofluidic Memristor. Nano Lett. 2024, 24, 12515–12521.

[12] Sun, W.; Xiao, Y.; Yan, P.; Sun, F.; Zhang, X.; Sheng, C.; Wang, Q.; Yu, Y. Observation of memristive behavior in PDMS-glass nanofluidic chip. Nano Res. 2025, 18, 94907098.

[13] Jahangeer, M.; Guo, J.; Qin, Z.; Li, C.; Liu, W.; Zhao, C.; Zhou, W.; Mou, H.; Wu, R.; Shen, C.; Fu, L.; Li, B.; Junaid, M.; Yao, H.; Wang, Q.; Du, G. Memory effects with broken symmetry in nanofluidic memristor for neuromorphic computing. Adv. Funct. Mater. 2026, e25932.